Eruption forerunners from multiparameter monitoring and application for eruptions time predictability (Piton de la Fournaise)

A. Schmid, J. R. Grasso, D. Clarke, V. Ferrazzini, Patrick Bachèlery, T. Staudacher

Eruption forerunners from multiparameter monitoring and application for eruptions time predictability (Piton de la Fournaise)

A. Schmid,[1] J. R. Grasso,[1] D. Clarke,[2] V. Ferrazzini,[3] P. Bachèlery,[4,5] and T. Staudacher[3]

Received 21 January 2012; revised 7 August 2012; accepted 27 August 2012; published 9 November 2012.

[1] Volcanic eruptions impact on societal risk, and volcanic hazard assessment is a necessary ingredient for decision-makers. However, the prediction of volcanic eruptions remains challenging due to the complexity and the non-linearity of volcanic processes. Identified forerunners such as increasing seismicity or deformation of the volcanic edifice prior to eruption are not deterministic. In this study, we use statistical methods to identify and discriminate precursory patterns to eruptions, on three sets of observables of Piton de la Fournaise volcano. We analyzed the short-term (i.e. the inter-eruptive period) time series of the seismicity rate, the deformation and the seismic velocity changes (deduced from seismic noise cross-correlations) over the period 1999–2006, with two main goals. First, we characterize the average pre-eruptive time patterns before 22 eruptions using superposed epoch analysis for the three observables. Using daily rate values, we resolve (1) a velocity change within 100–50 days from the eruptions onsets, then a plateau value up to eruption onset; (2) a power law increase in seismicity rate from noise level 15–10 days before eruption time; (3) an increase of displacement rate on the eruption day. These results support a three step mechanism leading to magma transfers toward the surface. Second we use pattern recognition techniques and the formalization of error diagrams to quantify the predictive power of each forerunner either as used independently or as combined to each other. We show that when seismicity rate alone performs the best prediction in the failure to predict versus alarm duration space, the combination of the displacement and seismicity data reduces the false alarm rate. We further propose a tool which explores the prediction results in order to optimize prediction strategy for decision-makers, as a function of the risk value.

Citation: Schmid, A., J. R. Grasso, D. Clarke, V. Ferrazzini, P. Bachèlery, and T. Staudacher (2012), Eruption forerunners from multiparameter monitoring and application for eruptions time predictability (Piton de la Fournaise), *J. Geophys. Res.*, *117*, B11203, doi:10.1029/2012JB009167.

1. Introduction

[2] Volcanoes are complex geophysical objects, often characterized by nonlinear dynamics [*Grasso and Bachèlery*, 1995; *Lahaie and Grasso*, 1998; *Melnik and Sparks*, 1999; *Sparks*, 2003], and by sensitive mechanisms to very small perturbations in which several processes are contemporaneously interacting [*Melnik and Sparks*, 1999; *Sparks*, 2003]. As a consequence, it makes challenging any effort either to model volcanic processes or to predict occurrence time, localization and volume of the next eruptions. Two approaches can be used to work on the prediction of eruptions timing, either on the long term behavior of a volcano, i.e. for periods larger than the inter-eruptive time [*Mulargia et al.*, 1985; *Marzocchi and Zaccarelli*, 2006; *Turner et al.*, 2008], or on the short term patterns. For both approaches, time, space and energy behaviors of different observables can be used [*Mulargia et al.*, 1991; *Sparks*, 2003; *Grasso and Zaliapin*, 2004; *Sandri et al.*, 2005]. In this study, we focus on the short-term approach, identifying the short-term patterns of three forerunners to impending eruptions on Piton de la Fournaise volcano, i.e. seismicity rate, deformation and seismic velocity changes.

[3] Several studies have focused on the geochemical and geophysical observables that precede volcanic eruptions, i.e. gas emissions, seismicity, ground deformation, in order to identify precursory patterns for volcanic eruptions. Among geochemical and geophysical forerunners, seismic event rate is the most used when attempting to forecast eruptions [*Kilburn*, 2003]. As pointed out by *Marzocchi et al.* [2008] and *Sparks* [2003] this short term approach has been

[1]Institut des Sciences de la Terre, Université de Grenoble, Saint Martin d'Hères, France.
[2]Institut de Physique du Globe, Paris, France.
[3]Institut de Physique du Globe, Observatoire Volcanologique du Piton de la Fournaise, La Plaine des Cafres, La Réunion, France.
[4]Laboratoire Géosciences Réunion, Saint-Denis, La Réunion, France.
[5]Laboratoire Magma et Volcans, Clermont-Ferrand, France.

Corresponding author: J. R. Grasso, Institut des Sciences de la Terre, Université de Grenoble, Batiment Géosciences, 1381 rue de la Piscine, FR-38400 Saint Martin d'Hères, France. (grasso@obs.ujf-grenoble.fr)

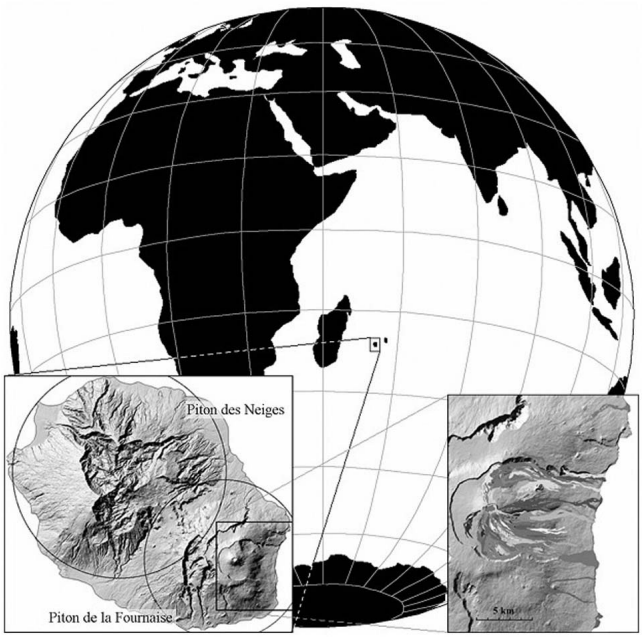

Figure 1. Geographic location of La Réunion island. (bottom left) La Reunion island showing the two main features, Piton des Neiges volcano on the West, and the currently active Piton de la Fournaise volcano on the east.

mostly studied by deterministic methods initiated by the fundamental law for material failure described by *Voight* [1988]. The majority of those deterministic approach however lack any possibility to evaluate the quality of the prediction. However, a probabilistic approach might be more efficient, due to the complexity and different precursory patterns for each eruption [*McGuire and Kilburn*, 1997; *Wadge and Isaacs*, 1988].

[4] Probabilistic approaches have been used on different volcanoes such as Asama [*Minakami*, 1960], Kilauea [*Klein*, 1984], Etna [*Mulargia et al.*, 1992; *Vinciguerra et al.*, 2001; *Marzocchi et al.*, 2004], or Piton de la Fournaise [*Grasso and Zaliapin*, 2004]. On Piton de la Fournaise volcano, *Stieltjes and Moutou* [1989] performed a statistical analyses of the eruption time series over the last 150 years in order to improve long-term predictability of eruptions. More recently, thanks to a statistical approach, *Collombet et al.* [2003] identified precursory processes using the VT seismicity over the period 1988–2001. They identified a power law increase of seismicity up to15 days prior to eruption. Since this pattern only appears when measured upon averaging (and might not exist for a single eruption), *Grasso and Zaliapin* [2004] tested the predictability of eruptions it generates by using a prediction algorithm based on pattern recognition techniques and the use of error diagrams.

[5] We are interested in extending the analysis of eruption predictability on Piton de la Fournaise in the framework of short-term statistics, using simultaneously 3 observables: seismicity rate, deformation and seismic velocity changes. *Peltier et al.* [2006] suggest that deformation of the volcanic edifice measured using an array of extensometers displays a precursory behavior up to several months before all the 14 eruptions of the period 1997–2003. *Brenguier et al.* [2008] managed to measure tiny seismic velocity changes prior to 5 eruptions using seismic noise cross-correlation techniques on the 1999–2000 period, and also propose those measurements as possible forerunners to eruptions on the 2000–2007 period.

[6] Therefore we chose to work on the time series of three different forerunners: the seismicity rate, the deformation and seismic velocity changes. We had two main goals:

[7] First, we analyzed the pre-eruptive behavior of the three forerunners, in order to extract time patterns and therefore to better constrain the mechanisms leading to magma transfers up to the surface.

[8] Second, following *Grasso and Zaliapin* [2004], we use the pattern recognition technique to quantify eruption predictability [*Mulargia et al.*, 1991]. This technique extracts information from the observation and provides a phenomenological picture without the need of any physical model [*Mulargia et al.*, 1991]. We applied this technique to the three previously defined forerunners and evaluate their predictive power either independently or as combined to each others. For that purpose we used the error diagrams introduced by *Kagan and Knopoff* [1987] and *Molchan* [1997]. This methodology has been first applied for eruption prediction by *Grasso and Zaliapin* [2004] on the seismicity of Piton de la Fournaise. The error diagrams are a useful tool to determine the whole set of possible solutions. Using alarm duration, failure to predict and false alarm rates, it provides tools that will help decision makers for risk assessment decisions.

2. Piton de la Fournaise Volcano

[9] The volcanic island "La Réunion" is situated in the South-Western Indian Ocean (Figure 1). It is a hot spot shield volcano of the hawaiian type, growing in an intra-plate environment, mainly constituted of basaltic rocks, estimated to be 540 000 years old [*Gillot and Nativel*, 1989]. It was build by the successive stacking of several shield volcanoes [*Bachèlery and Mairine*, 1990; *Merle et al.*, 2010]. *Courtillot et al.* [1986] showed that the hot spot at the origin of La Reunion island is also responsible of the formation of the Deccan trap volcanism (65 My), the Mascareignes basaltic shelf (35 My) and the Mauritius island (7–1 My). Piton de la Fournaise is the active volcano of La Réunion. It shows a strong eruptive activity with a nine months average return time for eruptions, during the 1900–2010 period. The mean eruptive volume rate estimated over one century is about $0.01\ km^3.yr^{-1}$ [*Lenat and Bachèlery*, 1987]. It is 10 times smaller than for the Kilauea hot spot volcano [*Dzurisin et al.*, 1984]. The current eruptive activity of Piton de la Fournaise is concentrated inside the caldeira of Enclos Fouqué (Figure 2) and the eruptive style is mostly effusive. In the last three centuries, only 7 or 8 eruptions (5% of the total number of recorded eruptions) occurred outside the Enclos Fouqué, and the lava flows destroyed forests, sugar cane and vanilla plantations, several houses and the main road [*Stieltjes and Moutou*, 1989]. Purely phreatic and magmato-phreatic explosions at the summit craters have been only observed in 1766, 1791, 1860, 1961, 1986 and 2007 [*Peltier et al.*, 2012]. Since most of the eruptions are small, effusive and mostly localized in uninhabited areas, Piton de la Fournaise does not represent a strong threat to the population. However, the vulnerability is increased by the high number of tourists on

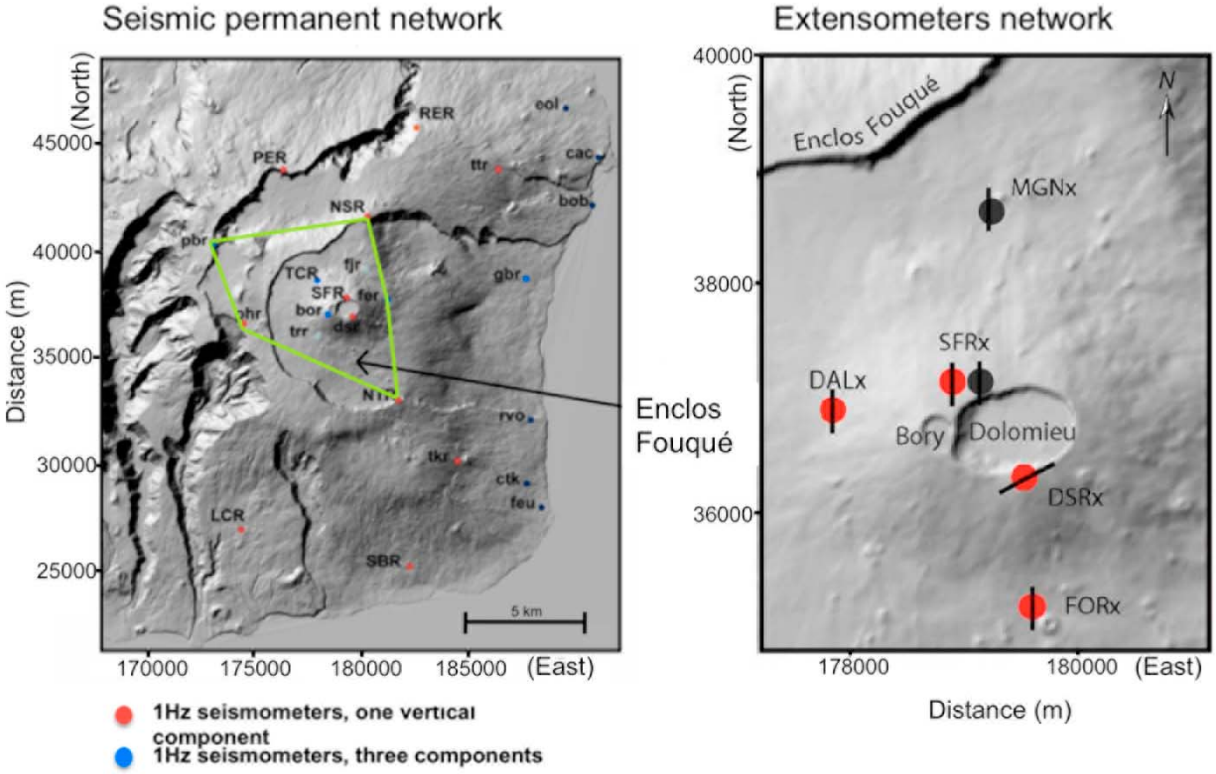

Figure 2. (left) Seismic and (right) extensometer networks on Piton de la Fournaise. In this study we used a daily seismic catalog from a daily counting of events over all seismic stations, and the data from extensometer FORx, south of the summital Dolomieu cone. We used the east-west component of the extensometer, which is perpendicular to local crack extension (the crack orientations are red bars on the map). The green polygon on the left figure delimits the area where the seismic stations are used for the computation of the seismic velocity changes (Gauss Laborde coordinates).

the volcano, the summit instability, and the risk for phreatomagmatic eruptions or eruptions outside the enclos Fouqué, as it occurred in the past. Its numerous eruptive episodes and the available data from the volcano monitoring since 1980 by the Volcanological Observatory (OVPF), make this volcano a perfect test laboratory for prediction schemes.

3. Three Eruptions Forerunners: Seismicity Rate, Deformation Rate and Seismic Velocity Changes

3.1. The Daily Data Over the 1999–2006 Period

[10] Different arrays of geophysical or geochemical instruments are deployed on Piton de la Fournaise since the 80's. In Figure 2, we show the permanent seismic network (left) and the permanent extensometers network (right).

[11] The OVPF seismic catalogue is built on daily manual detection of seismic events (1988–2011). An event is included into the catalog when the signal is recorded on more than three stations. The seismicity at the Piton de la Fournaise volcano is mainly composed of volcano-tectonic (VT) events and rockfall signals. Those VT events are associated with rupture or displacement along faults. Their frequency is typical of tectonic earthquakes and the VT waveform shows clear P and S wave arrivals (see *McNutt* [2002] for a review on the seismic signals associated with volcanoes). Very few long-period (LP events) are ever recorded on Piton de la Fournaise [*Aki and Ferrazzini*, 2000] including in the 1999–2007 period. The VT events are usually associated with shear failure or slip on faults: their frequency content is typical of tectonic earthquakes, with clear P and S phase onsets [*Minakami*, 1960; *Chouet*, 1996; *McNutt*, 2002]. VT events are considered as a sign of renewed volcanic activity since they are usually contemporary to volcano processes [*McNutt*, 2002]. On Piton de la Fournaise, this local seismicity ($M_w < 3$) has been related to damage processes occurring during magma transfers, such as the overpressure in the magmatic chamber or the propagation of a dike [*Grasso and Bachèlery*, 1995; *Sapin et al.*, 1996; *Aki and Ferrazzini*, 2000]. Seismicity is the most used candidate to monitor volcanoes worldwide.

[12] For the last 30 years, the OVPF has been monitoring the Piton de la Fournaise volcano, and daily deformation data are available. The inflation of the volcanic edifice leads to surface deformations, measurable through either opening of fractures, variations of the slope tilt or single point displacement values. On Piton de la Fournaise, the deformation on the edifice is measured from different networks of geophysical equipment: extensometers, tiltmeters, and GPS arrays. We chose to use only the measurements from one extensometer located at the base of the summit cone (see FORx on Figures 2 and 3 for on-site instrument), because it showed the longest recording period and it is

Figure 3. FORx extensometer located at the base of the summit crater of Piton de la Fournaise. The length of the crack is about 10 m and the opening of the crack is around 2 cm.

suggested to be the most sensitive to pre-eruptive deformation of the volcano edifice [*Bachèlery et al.*, 2001; *Peltier et al.*, 2006]. This very local measure along a single crack may not characterize the whole volcanic edifice, however some local circumstances drive a positive concomitance of the measurement together with the eruption and we therefore consider this observable as a forerunner. The available data are the daily value of a crack opening, in mm, over the period 1997–2007.

[13] *Brenguier et al.* [2008] showed that from the cross-correlation of ambient seismic noise, one could retrieve tiny changes in the seismic velocity changes under the volcanic edifice. When applied on the Piton de la Fournaise (1999–2000) this technique suggests that a decrease of the seismic velocities occurs a few days before eruptions. These variations in the seismic velocity are suggested by *Brenguier et al.* [2008] to be driven by stress changes related to increase of magma pressure in the magma storage zone or due to opening cracks [*Duputel et al.*, 2009]. For our analysis we use the daily values of the seismic velocity for the period 1999–2006. The velocity changes are estimated on 0.1–1 Hz filtered data. For each station pair, a daily data is computed as the averaged change in seismic velocity on the 10 days that precedes the nominal day. The daily values used in this study are averaged on all the seismic stations pairs included in the green polygon of Figure 8 (left). The velocity changes imaged through this technique characterize the medium below those stations. Ongoing work is undertaken to localize more precisely the location of those seismic variations.

[14] In order to be able to compare the three forerunners on the same data set of eruptions, we chose the common period of the available data. Therefore, the following study is performed on the 06-23-1999 – 12-31-2006 period.

[15] Before most eruptions, we observe a clear increase of either the seismicity, displacement or seismic velocity variations (Figures 4, 5, and 6). For instance the July 2000

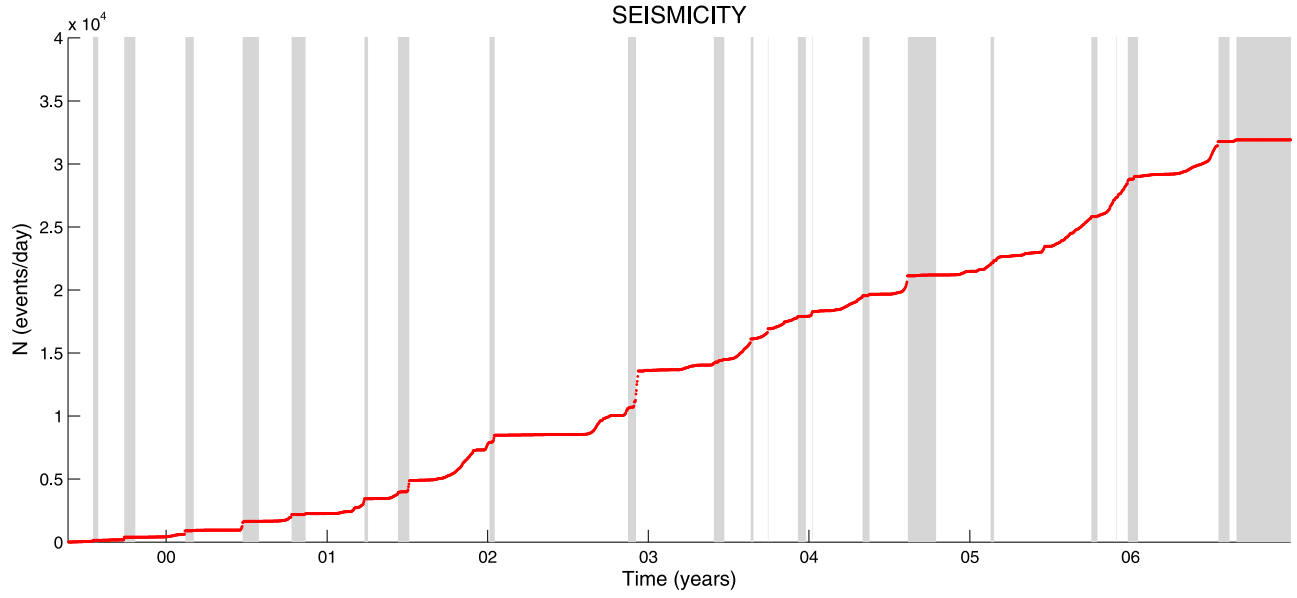

Figure 4. Temporal evolution of the daily cumulative VT event rate, 1999–2006. Grey areas represent periods of eruption.

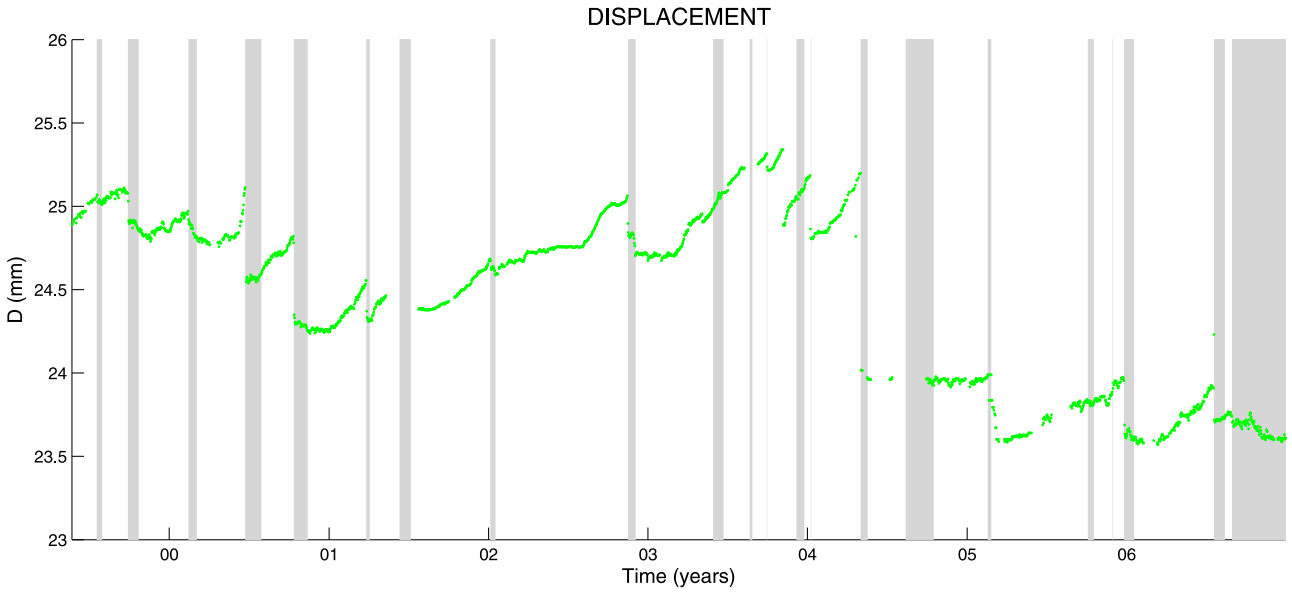

Figure 5. Temporal evolution of the daily cumulative displacement recorded on the extensional component of extensometer FORx, 1999–2006. Grey areas represent periods of eruption.

eruption shows increases of the three observables before the eruption (Figure 7). However, this observation is not systematic for all eruptions. It is the reason why we look at the data from a statistical viewpoint, by averaging a mean pre-eruptive behavior of the observables for the 22 eruptions of the 1999–2006 period.

3.2. Forerunners Patterns

[16] To study the mean behavior of the three forerunners to eruptions, we stacked the daily rates and cumulative data over [−200; 200] days windows centered on eruption time, for the 22 eruptions occurring in 1999–2006 (Figures 8 and 9 for daily rate and cumulative data respectively). This 200 days interval corresponds to the mean inter-eruption time. This stack technique, previously used [*Collombet et al.*, 2003; *Lemarchand and Grasso*, 2007], allows us to extract characteristic averaged patterns, which are not always seen for a single eruption. We tested that the identified characteristic trends are not driven by a single time series using a bootstrap analysis (the test results are shown in Figure S1 in the auxiliary material).[1]

[17] As previously shown by *Collombet et al.* [2003] over the period 1988–2001, we confirm a mean accelerating

[1]Auxiliary materials are available in the HTML. doi:10.1029/2012JB009167.

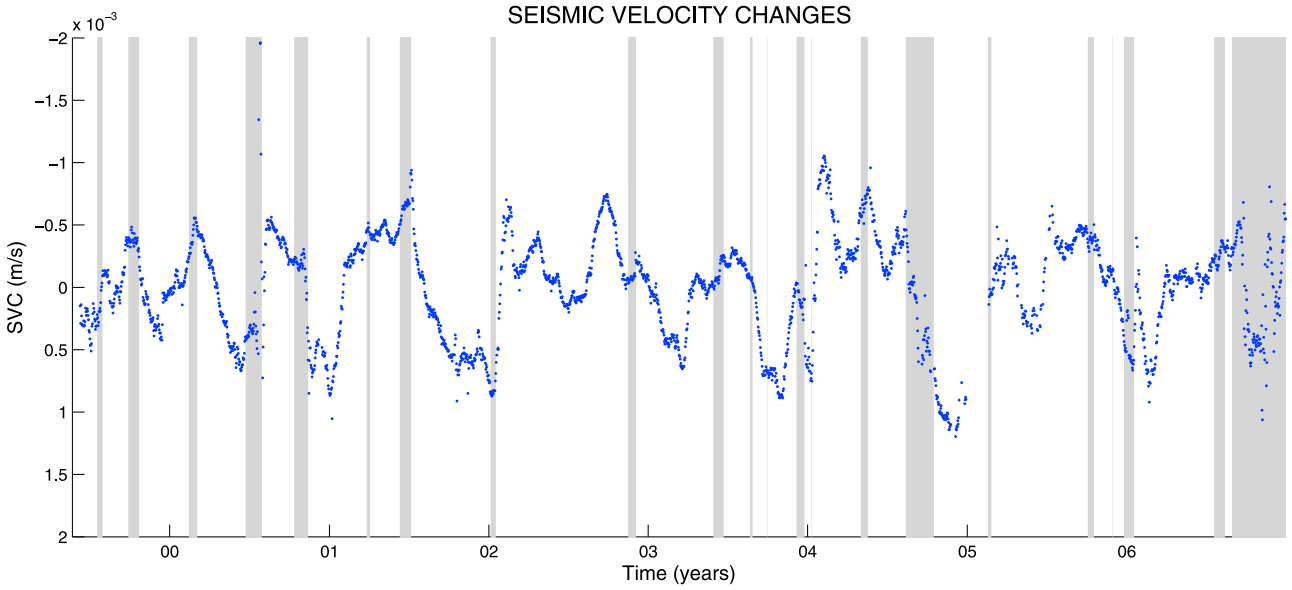

Figure 6. Temporal evolution of the daily cumulative seismic velocity change computed using cross-correlations of ambient seismic noise, 1999–2006. Grey areas represent periods of eruption.

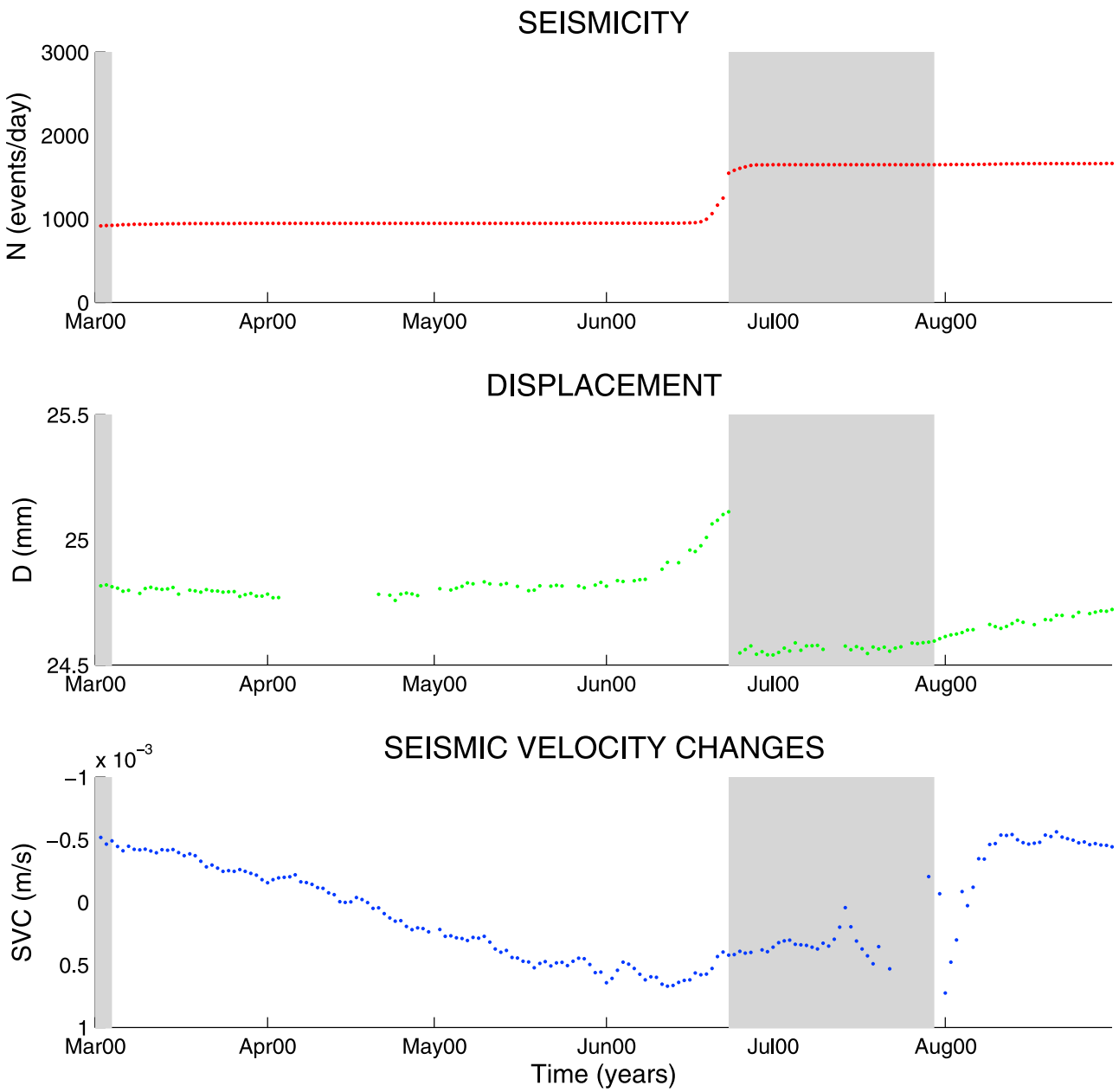

Figure 7. Temporal evolution of the three forerunners around July 2000 eruption. (top) Daily cumulative VT event rate; (middle) daily cumulative displacement recorded on the extensional component of extensometer FORx; (bottom) daily cumulative seismic velocity change computed using cross-correlations of ambient seismic noise. Grey areas represent periods of eruption.

pattern appears when stacking the pre-eruptive daily seismic sequences prior eruptions over the period 1999–2006. This acceleration starts about 10 days prior eruption (when the seismic rate increases above noise level). The linear trend of the seismicity in the log-log plot confirms that this accelerating pattern follows a power law (Figure 8a, right).

[18] When analyzing individual eruptions, *Peltier et al.* [2006] suggested that an increase of the cumulative displacement is observable more than three months before eruptions. On the cumulative displacement, we recover this linear increase up to 200 days before eruption (Figure 9). There is a possible change in the slope around 100 days before eruptions. When analyzing the pattern as daily rates on average for all eruptions (Figure 8b), we observe that the opening rate of the crack, i.e. the derivative of the function used by *Peltier et al.* [2006], significantly increases only one day before eruptions (Figure 8b). Analysing individual eruptions at Kilauea, *Bell and Kilburn* [2012] also find a constant rate of surface deformation before eruptions.

[19] For the seismic velocity changes, it is possible to identify a mean decrease in seismic velocity changes rate, above noise level, 100 to 50 days before eruption (Figure 8c). Then a flat plateau value is resolved for the last 50 days, which inhibits any time prediction. Consequently,

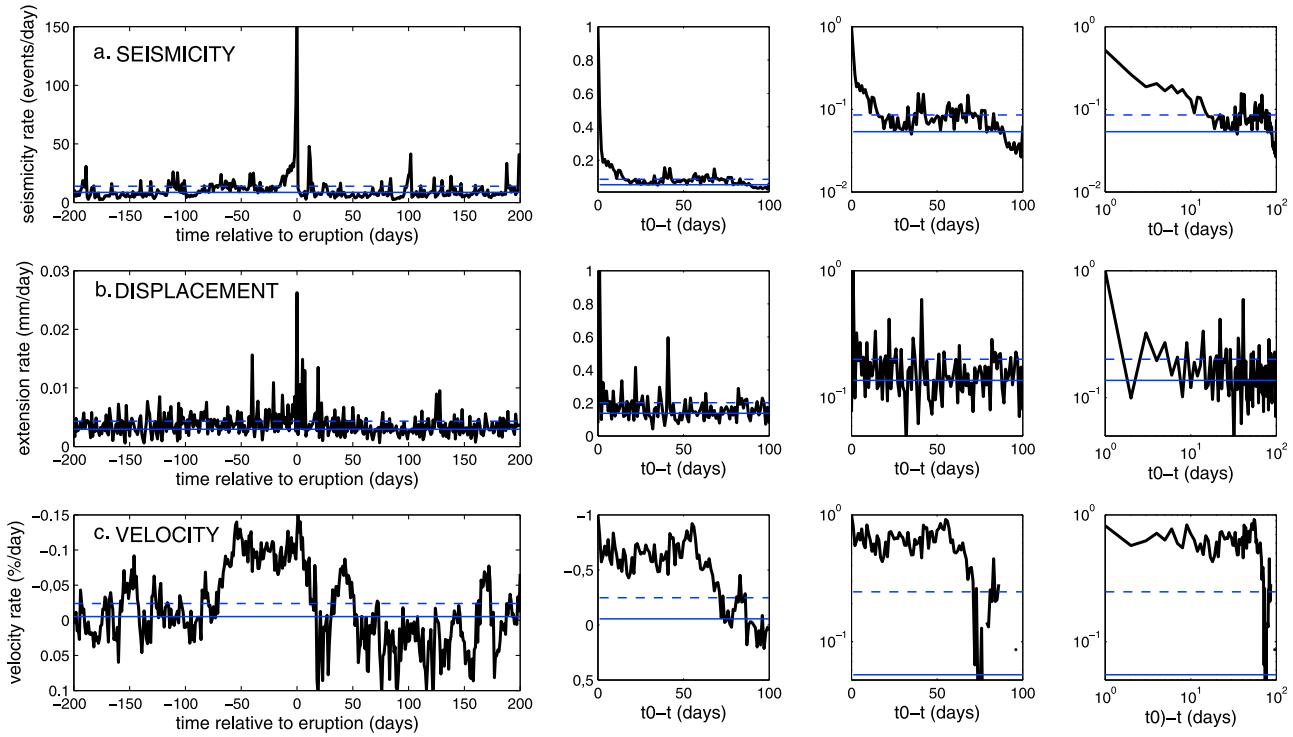

Figure 8. Stacked daily rates over [−200, 200] days windows around the 22 eruptions. t = 0 corresponds to eruptions onsets. Data before eruption, as a function of $(t_0 - t)$, either in normal, lognormal or loglog plot to outline any linear, exponential or power law tendency, from left to right respectively. We go closer to the eruption time when going toward the left of the time axis. On all diagrams blue plain lines and blue dotted lines are background level computed over a [−400; −100] days window before eruptions and standard deviation respectively. (a) Seismicity rate (as the number of event per day); (b) displacement rate (as the daily opening of a sensitive crack); (c) seismic velocity changes (as the daily variation of the seismic velocity).

the analysis of the seismic velocity changes as a cumulative data shows a linear increase 50–100 days before eruptions (Figure 9c).

[20] The different characteristic times, and the different laws governing pre-eruptive behaviors for the three forerunners raise the question of common pre-eruptive mechanism leading to such asynchronous patterns. Whatever the pre-eruptive processes that drive the observed patterns, the characteristic times for change before eruptions imply a possible predictive power for each observable.

4. Predictability of Eruptions

4.1. Pattern Recognition and Error Diagrams

[21] Within the framework of complex systems, we follow a pattern recognition approach to explore the predictability of Piton de la Fournaise eruptions (*Keilis-Borok* [2002] for a review). The prediction algorithm is quite simple, and based on the detection of a threshold value on the time function of a given forerunner (Figure 10). This function, Φ, can be written as

$$\Phi(t, t_w) = \sum_i \frac{\phi_i}{t_w} \qquad (1)$$

where t_w is the variable window length (as one of the input alarm parameters). For our data sets, Φ will be successively the VT earthquake rate (with ϕ_i being the observed number of VT events in the time window [t-t_w, t]), the displacement rate (with ϕ_i being the displacement measured on the time window [t-t_w, t]), and the seismic velocity changes rate (with ϕ_i being the seismic velocity change over the time window [t-t_w, t]). An alarm is detected when $\Phi(t, t_w) \geq N_\Phi$, where the threshold N_Φ is an adjustable parameter. We use this function to predict whether an eruption will occur in the time interval $[t, t + \Delta]$. If $\Phi(t, t_w) \geq N_\Phi$, we declare an alarm for the time interval Δ. The alarm is relieved either after the eruption occurred, or when the Δ time window has expired [*Grasso and Zaliapin*, 2004]. Therefore, our prediction scheme depends on three alarm parameters: (1) the time window t_w over which the precursory process $\Phi(t, t_w)$ is computed, (2) N_Φ the threshold for the precursory parameter over which an alarm is declared, and (3) the time window Δ over which the alarm is declared.

[22] It is necessary to evaluate the quality of the prediction considering not only the rate of successful prediction but also the rate of false alarms it generates and the total duration of the alarms. Those two last outputs are the "cost" to achieve a given rate of successful predictions. For that purpose, we used the "error diagrams", introduced in

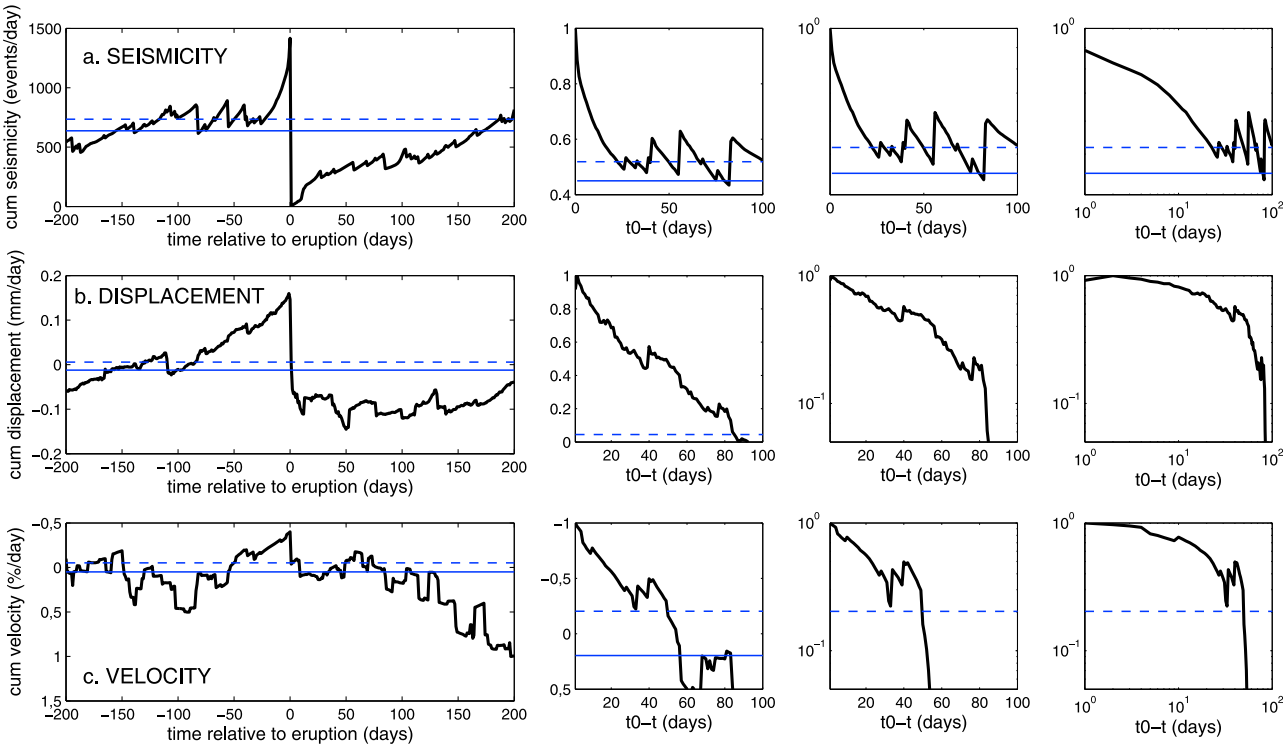

Figure 9. Stacked cumulative data for the 22 eruptions over [−200, 200] day windows around eruption time: t = 0 corresponds to eruptions onsets. After the end of each eruption, we reset each observable values back to 0. Data before eruption, as a function of $(t_0 - t)$, either in normal, lognormal or loglog plot to outline any linear, exponential or power law tendency, from left to right respectively. We go closer to the eruption time when going toward the left of the time axis. On all diagrams blue plain lines and blue dotted lines are background level computed over a [−400; −100] days window before eruptions and standard deviation respectively. (a) Cumulative seismicity (as the number of events); (b) cumulative displacement; (c) cumulative seismic velocity changes.

seismology by *Kagan and Knopoff* [1981] and *Molchan* [1997]. The formalization of error diagrams allows us to characterize the performance of prediction outcomes using the rate of success, the rate of false alarms, and the total duration of alarms. When calling A the number of declared alarms , A_f the number of false alarms, N_e the number of eruptions that occurred, A_s the number of successful predictions, A_m the number of missed events, and Φ_Δ the time covered by the alarms, the three dimension-less results of the prediction can be defined as follows:

- the rate of failures to predict $f_p = A_m/N_e$
- the rate of false alarms $f_a = A_f/A$
- the total duration of alarms $\tau = \Phi_\Delta/T$ where T is the duration of the whole considered period.

[23] The values of τ, f_p and f_a, when mapped on the two error diagrams, allow us to compare the efficiency of any prediction, depending on the three alarm parameters t_w, N_Φ and Δ (Figure 12).

4.2. Predictability of the Eruptions Using Three Forerunners of Piton de la Fournaise

4.2.1. Single Forerunner Prediction

[24] In a first step, we applied the pattern recognition algorithm and designed the error diagrams for the three single forerunners (seismicity, displacement and seismic velocity

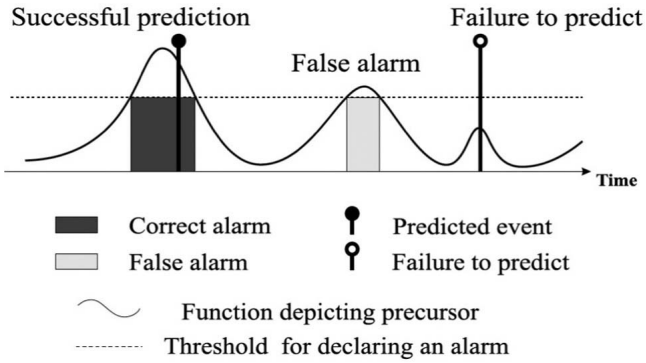

Figure 10. Prediction scheme and prediction outcomes. We defined an alarm threshold over a time function which is our prospective precursor. Three outcomes may occur. (1) The alarm is triggered and an eruption occurs. This is a successful prediction. (2) An alarm is triggered but no eruption occurs. This is a false alarm. (3) An eruption occurs but no alarm has been triggered. This is a missed event, i.e. a failure to predict case. From *Grasso and Zaliapin* [2004].

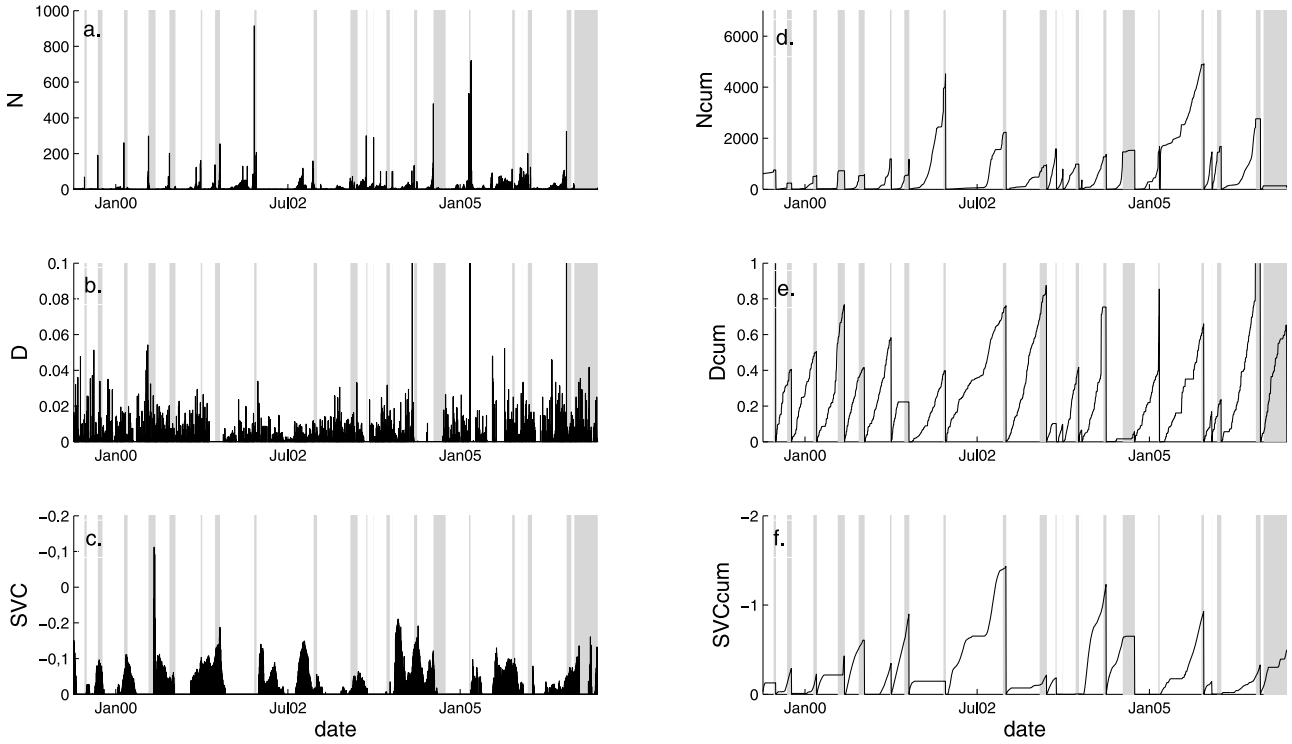

Figure 11. Time evolution of the 3 observables, with two functions per observable: (a) daily seismic rate, (b) daily displacement rate, (c) daily seismic velocity changes rate, (d) cumulative seismicity, (e) cumulative displacement, (f) cumulative seismic velocity changes. To predict the time to the next eruption using the cumulative data (Figures 11b, 11d and 11f), we reset the values back to 0 the day after the end of each eruption. The grey vertical bars indicate periods of eruptions.

changes), either using the daily or the cumulative rates. For the cumulative data sets, we further imposed the function back to 0 after each eruptions (Figure 11).

[25] The alarm parameters we tested as inputs for pattern recognition are summarized in Table 1.

[26] Figure 12 shows the results of prediction displayed in the error diagrams for the seismicity rate.

$$D_{\min} = \min\left(\sqrt{\alpha(f_p(t_w, N_\Phi, \Delta))^2 + \beta(f_a(t_w, N_\Phi, \Delta))^2 + \gamma(\tau(t_w, N_\Phi, \Delta))^2}\right) \quad (2)$$

[27] The error diagrams represent all the possible prediction outcomes for all the values of the alarm parameters we explored (Table 1). On the left diagram of Figure 12, the diagonal is the result of a random guess prediction strategy (the points representing the prediction results would be aligned on this diagonal). Consequently, the larger the distance from the diagonal in this diagram, the larger the departure from a random prediction, for the tested combination of alarm parameters. Because a low failure to predict rate will have a cost in terms of false alarms and total alarm duration, we propose a tool to help the decision makers to extract optimum prediction (i.e. the combination of alarm parameters) for a given prediction strategy. This prediction strategy will depend on the local vulnerability of the volcanic area. As a first step application, our target is the closest point from the origin points of each diagram of Figure 12 (i.e. the furthest from the diagonal) when considering the three diagrams, simultaneously. Mathematically, it corresponds to minimizing the three prediction outputs simultaneously. The decision-maker can favor some of the prediction outputs (missed event rate, false alarm rate or total alarm duration) by using α, β and γ weighting coefficients. We defined $D_{\min}$ as:

Table 1. The Alarm Parameter Values Tested for Pattern Recognition on the Different Data Sets[a]

t_w (days)	1:1:5
Δ (days)	1:5:100
N_s (events/day)	1:5:100
N_{scum} (events)	1:50:1000
N_d (mm/day)	10^{-3}.(1:2:40)
N_{dcum} (mm)	(1:50:1000).10^{-3}
N_{svc} (%/day)	(1:1:20).10^{-2}
N_{svccum} (%)	(1:50:1000)10^{-3}

[a] t_w is the time window used to compute the N_i threshold values for alarm onset. Δ is the alarm duration. N_s (seismicity), N_{scum} (cumulative seismicity), N_d (displacement), N_{dcum} (cumulative displacement), N_{svc} (seismic velocity changes), N_{svccum} (cumulative seismic velocity changes) are the threshold over which an alarm is declared.

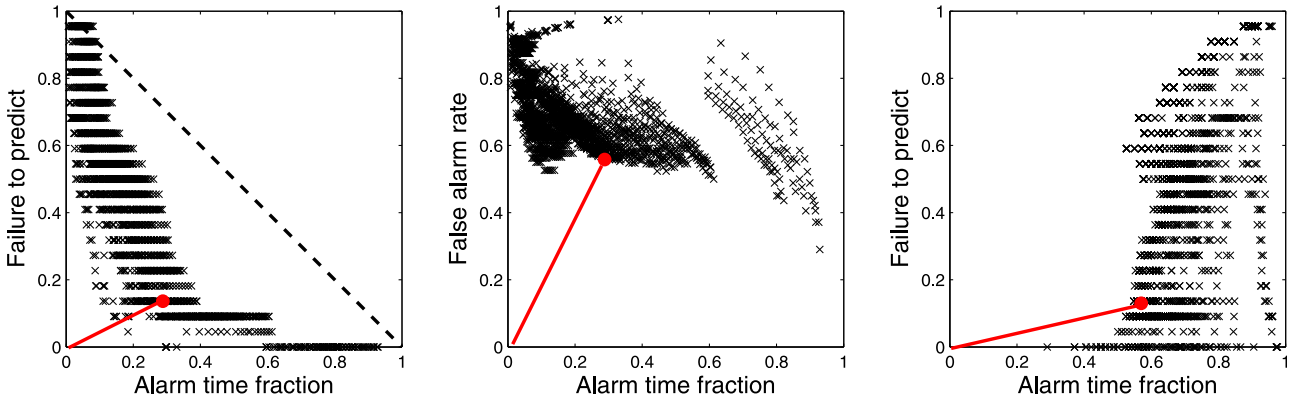

Figure 12. Error diagrams for the daily seismicity rate alone. From left to right, failure to predict versus alarm time fraction, false alarm rate versus total alarm duration, failure to predict versus false alarm rate. Each black point corresponds to the prediction output given one set of alarm parameters (t_w, N, Δ). With the discrete step we used, we explored 2000 (5*20*20) combinations for the three parameters tested under pattern recognition. The error diagrams image all the 2000 prediction outcomes we tested. The dotted line on the left diagram is the expected outcome space for a random guess prediction strategy. The red point corresponds to the optimum prediction outcome (i.e. the set of alarm parameters minimizing the D-value defined in equation (2)). The red lines are the distance to origin point for this specific prediction output.

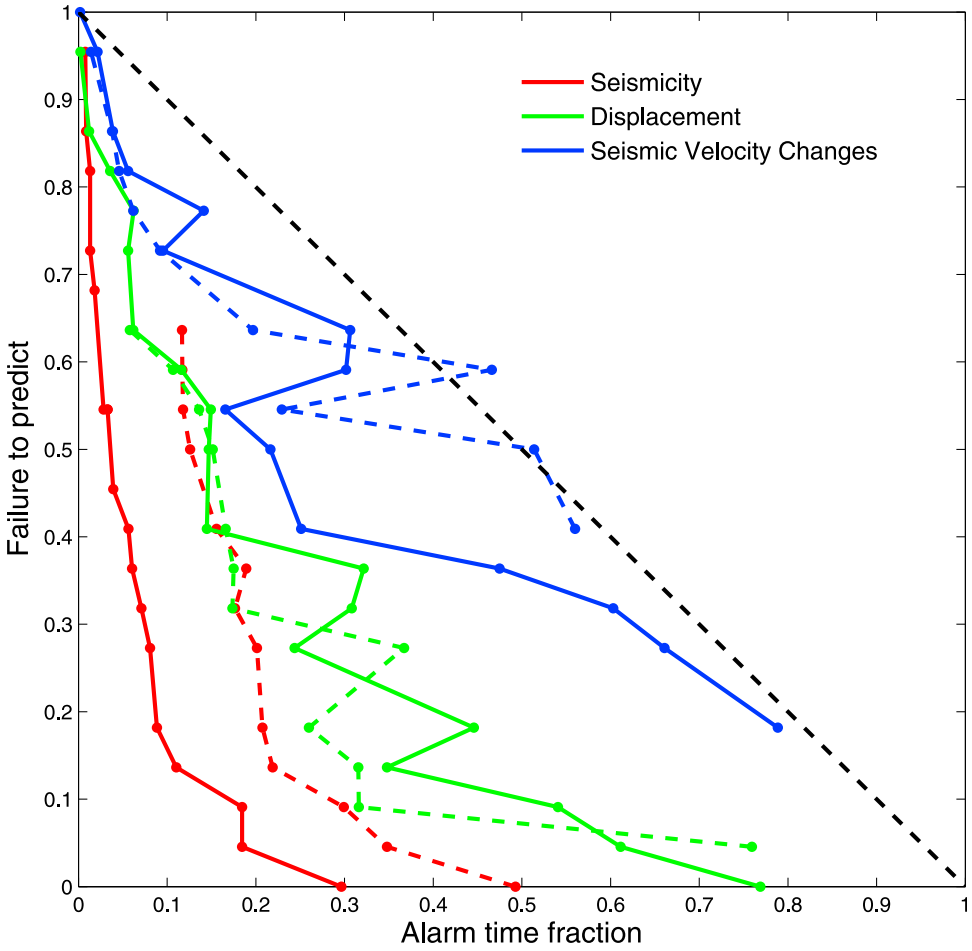

Figure 13. Envelops of the prediction outputs in the failure to predict versus alarm time fraction diagram for the 3 forerunners, when minimizing equation (2). Plain lines are the rate values, dotted lines are the cumulative values.

Table 2. Prediction Outputs for the Combinations of Forerunners We Considered[a]

	$D_{\min}$	t_w	Δ	N_s	N_d	N_{svc}	f_p	f_a	τ
s	0.61	1	41	46	-	-	18.18%	40.00 %	42.69%
s_{cum}	0.59	4	36	801	-	-	36.36%	26.32%	39.74%
d	0.55	4	96	-	11	-	22.73%	32.00%	38.97%
d_{cum}	0.50	1	36	-	71	-	18.18%	14.29%	45.05%
svc	0.85	5	81	-	-	14	30.00%	44.00%	45.43%
svc_{cum}	0.83	5	41	-	-	301	45.00%	54.17%	41.66%
s_{cum} OR d_{cum}	0.56	4	36	751	51	-	22.73%	29.17%	43.34%
s_{cum} AND d_{cum}	0.44	1	31	301	11	-	22.73%	22.73 %	30.31%

[a]In the left column, s refers to seismic rate, s_{cum} refers to cumulative seismicity, d refers to displacement rate, d_{cum} refers to cumulative displacement, svc refers to seismic velocity changes rate and svc_{cum} refers to cumulative seismic velocity changes. $D_{\min}$ is the minimum value as described in equation (2). t_w, Δ, N_s, N_d, N_{svc} give the values of the alarm parameters (Table 1) associated with the values of $D_{\min}$. The three last columns give the corresponding prediction results.

where f_p is the missed event rate, f_a is the false alarm rate and τ the alarm time fraction when exploring all possible values of input alarm parameters t_w, N_Φ and Δ. For this first step application, we use $\alpha = \beta = \gamma = 1$.

[28] Figure 13 displays the minimum envelops (i.e. the furthest outcomes from the random prediction outcomes) of the prediction outputs in the missed event rate versus alarm time fraction diagram, for the 6 functions previously defined.

[29] Figure 13 shows that for the six data sets, many points (i.e. prediction results given different combinations of alarm parameters) are below the diagonal. This statistically confirms that the prediction results obtained for all the considered data sets perform better than random, i.e. the three observables taken as rate or cumulative functions have predictive performances. We also note that the seismicity shows points further from diagonal than deformation or seismic velocity changes. It favors seismicity to be more efficient than deformation or seismic velocity changes when considering only failure to predict results. However, if we take simultaneously into account all prediction results (including false alarm rate) through the optimum point defined in equation (2), the cumulative displacement emerges as the best candidate regards to our prediction strategy with $\alpha = \beta = \gamma = 1$ (Table 2 and Figure 14).

[30] The optimum for the cumulative deformation, and therefore the best prediction results in our strategy, corresponds to a missed event rate of 18% and the lowest false alarm rate at 14%. It corresponds to a displacement threshold of 0.71 mm since the previous eruption, and an alarm duration of 36 days. For cumulative displacement values, the gain to minimize the D-value defined in equation (2), relatively to the others forerunners, emerges from a lower false alarm rate (Figure 14).

4.2.2. Prediction From Forerunners Combinations

[31] Another target of this study is to test the relative performance of the combination of the forerunners in a prediction scheme. For this purpose we run the same prediction algorithm as previously but using conditional combinations on forerunners patterns for the triggering of alarms. The logical link between the two conditions may be either "AND" or "OR". An "AND" link will tend to allow lower false alarm rates whereas a "OR" link will tend to improve failure to predict.

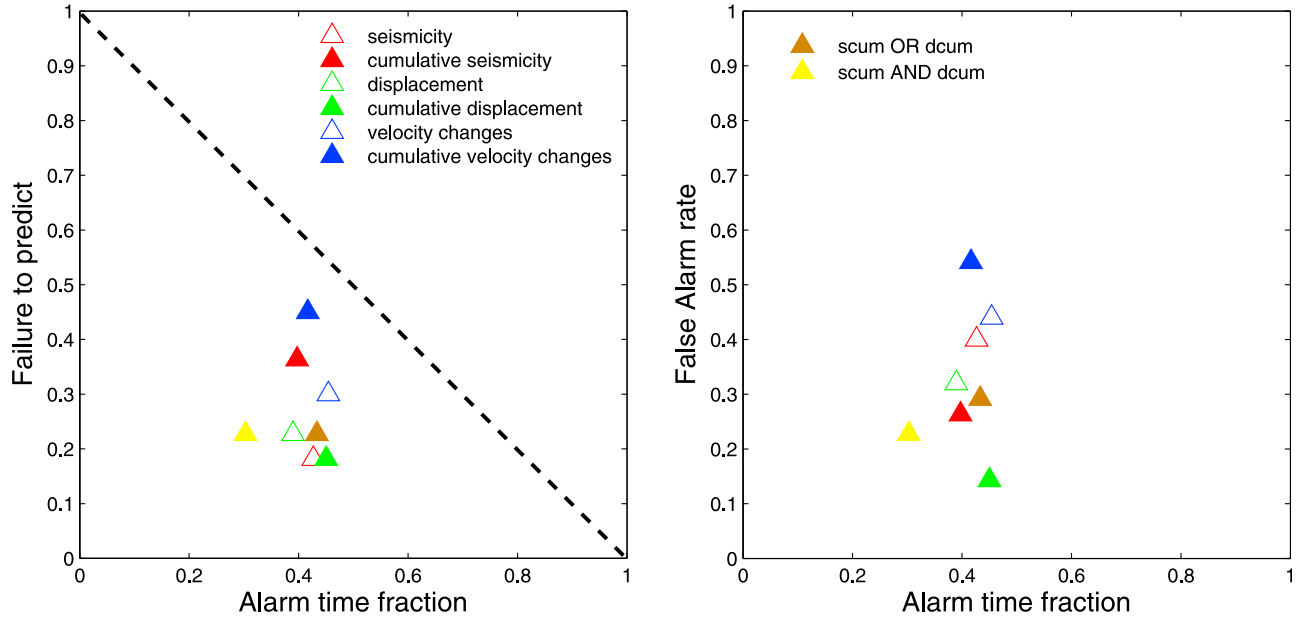

Figure 14. Prediction outputs for the different observables when using $D_{\min}$ as defined in equation (2). Red is seismicity, green is displacement and blue is seismic velocity changes. Open and plain markers are used for the discrete and cumulative data respectively. Brown and yellow are used for the combinations of cumulative seismicity and cumulative displacement (respectively AND and OR combinations, Figure 15).

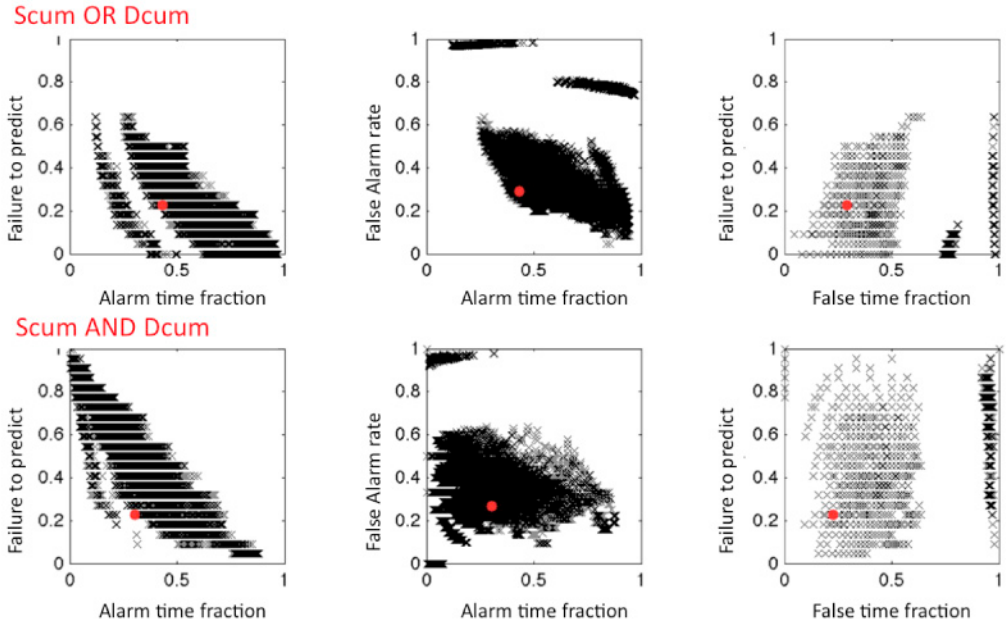

Figure 15. Error diagrams from combining seismicity and deformation data. (top) Seismicity OR deformation; (bottom) seismicity AND deformation. The red dots correspond to the optimum points as defined in equation (2).

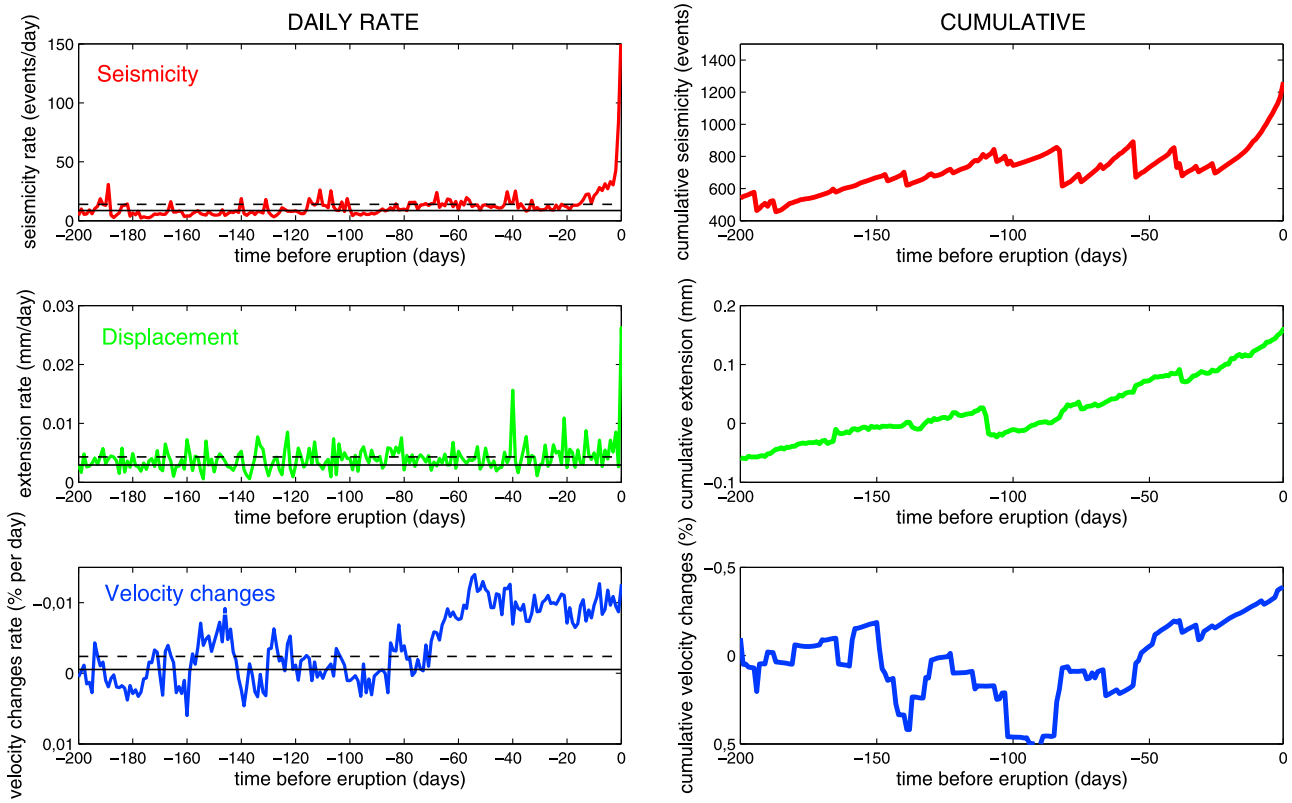

Figure 16. Comparison of the normalized stacked pre-eruptive patterns of the three forerunners: seismicity, displacement and seismic velocity changes, 1999–2006, 22 eruptions, as (left) daily rates and (right) cumulative data.

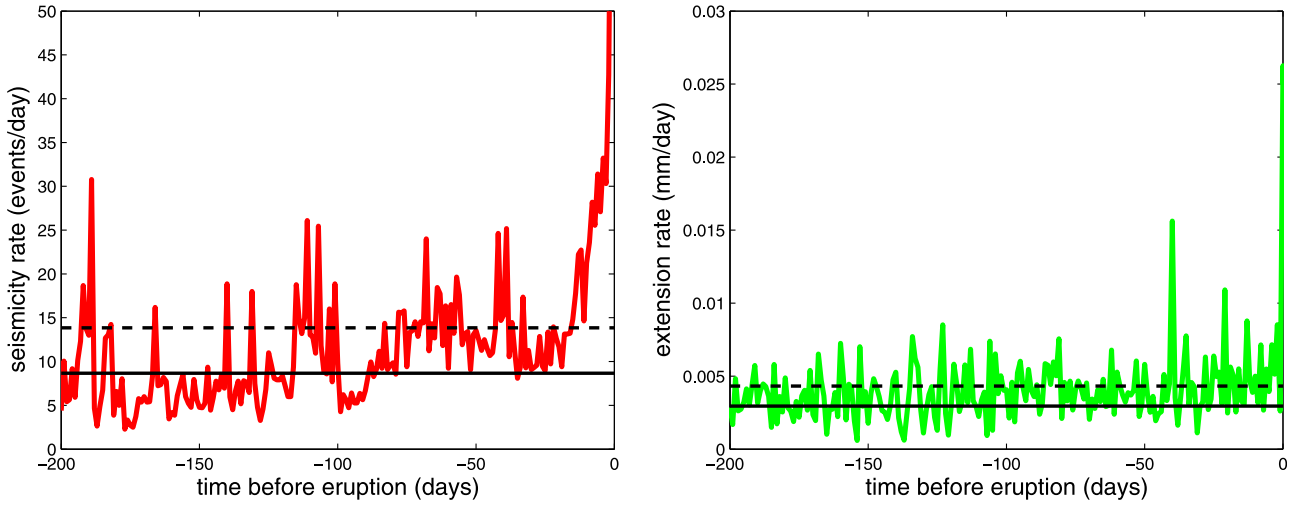

Figure 17. Stacked pre-eruptive patterns of the seismicity rate and the displacement rate (red and green respectively), 1999–2006, 22 eruptions. Plain black line is the background value computed over a [−400; −100] days window before eruptions. Dotted black line is the standard deviation.

[32] From the performances of independent prediction skills (Table 2), we chose to work only with the two best candidates for prediction, i.e. cumulative seismicity and deformation. Therefore, we explored a combined prediction for cumulative seismicity and the cumulative deformation (Figure 15).

[33] At first sight, the "cumulative seismicity AND cumulative deformation" results (lower diagrams of Figure 15) show that the best performance in the failure to predict space is largely dominated by the "only seismicity" results (Figure 12). However, when we consider the second error diagrams, the number of false alarm is dominated by the "only deformation" results. As a result when calculating the optimum point for the different combinations, we find that cumulative seismicity AND cumulative deformation allows a smaller D-value (see equation (2)), i.e. 0.44 and 0.88 for AND and OR predictive schemes, respectively (Table 2). It means that in our definition of the predictive power of any given forerunner sets (allowing the smallest distance as defined in equation (2)), we improve the prediction results when using combinations of observables, by decreasing the false alarm rate.

[34] It is important to note that those results emerge from choices on both an optimum point to compare the prediction outputs, and the weights used to combine the forerunners in the prediction algorithm. In the definition we used for optimum prediction (with $\alpha = \beta = \gamma = 1$), we find that cumulative deformation is the best candidate, and that we can improve the prediction when combining cumulative seismicity and cumulative deformation (Figure 14 and Table 2). The alarm parameters corresponding to this optimum point (Table 2) allow almost 80% of successful prediction with only 22% of false alarms and 30% of time under alarm.

5. Discussion and Conclusions

5.1. Constrains on the Pre-eruptive Process From Average Forerunner Patterns

[35] It is known that the deterministic forecast of eruption time is not yet achieved by the geoscientist community [e.g. *Voight*, 1988; *Chouet*, 1996; *McNutt*, 1996]. As a first simplification test of the forecast problem, we used superposed epoch analysis for seismicity rate, surface displacement and seismic velocity change. This approach hypothesizes that there are common patterns before eruptions. Fluctuations around this mean common pattern are supposed to be second order patterns associated with the local volcano heterogeneity (e.g. either within the passive volcano property of rock matrices or as embedded in a deviation from a simple process that leads toward eruption). For the Piton de la Fournaise volcano, using signals before 21 effusive eruptions, the 3 observables we considered display non-homogeneous patterns (Figures 8, 16, and 17). The major signal for the daily seismicity rate emerges as a peak value for seismicity rate 1–2 days from eruption day (Figure 8). As highlighted by the log-log plot on Figure 8a, this climax peak value is the final trend of a continuous power law increase that is resolved above the noise level 15 days before the eruption days. The displacement data, which corresponds to a local crack opening at the surface of the volcano, estimates volcano surface changes (inflation of the edifice prior to eruptions). This measurement captures shallow phenomena as compared to seismicity rate that encompasses seismicity located within 0–5 km depth range [e.g. *Aki and Ferrazzini*, 2000; *Battaglia*, 2001]. The signal fluctuations during the 50 days before eruption days are large. However, a clear increase of the displacement rate occurs the day of eruption with a peak value above background level and standard deviation. In the log-log plot (Figure 8b), we observe a possible power law increase, if any, within 8–10 days from the eruption day, however dominated by large fluctuations. The change in seismic velocity displays lower frequency changes relatively to the two previous observables (Figure 8c). The eruptions are preceded by a decrease in velocity change in the 70–50 days window before the eruption day. Then the velocity change remains constant at its strongest plateau value during the last 50 days before eruptions. We do not resolve accelerating pattern at shorter timescale before eruptions (Figure 8c). Note that the high frequency fluctuations during

the larger amplitude and lower frequency changes in seismic velocity prevent the low frequency signal to be efficient in the prediction scheme we used.

[36] From these three observables, a possible coupling emerges between seismicity rate and crack aperture but the change in velocity appears to capture independent longer time patterns. Merged together as daily rate values, these stacked data support a three-step process as a mean field volcano dynamics before eruption.

[37] First, the seismic velocity change within 70–50 days from the eruptions onsets is followed by a plateau value up to eruption onset. The decrease in velocity is proposed to be the signature of in-depth cracks opening due to stress changes within the volcano [*Brenguier et al.*, 2008]. It may support a change in the magma storage volume as driven by pressure increase due to either crystallization process or new reservoir feeding from depth (e.g. *Lahaie and Grasso* [1998] for a conceptual model of upper volcano dynamics). The seismic velocity changes suggest a progressive increase in the magma storage forcing (70–50 days before eruptions), then a rough constant forcing rate for the last 50 days. Note that the 70–50 days timescale roughly corresponds to the timescale proposed by *Peltier et al.* [2006] for the possible deterministic forerunner pattern using surface crack opening only, considering the 14 eruptions on the 1997–2003 period. However, using Figure 8 we do not resolve, in the 100–50 day window before eruptions, any mean pattern above noise level for displacement values using the 21 eruptions on the 1999–2006 period.

[38] Second, during the 50 days constant forcing phase from the storage area, a power law increase in seismicity rate is resolved above the noise level 15 days before eruption time. This power law increase in seismicity rate is also recurrent on both 1988–2001 [*Grasso and Zaliapin*, 2004], and 1998–2003 [*Collombet et al.*, 2003]. This observation, which is suggested to map the brittle damage before failure, argues for a brittle damage of the reservoir wall through time [e.g. *Grasso and Zaliapin*, 2004]. This brittle damage is recorded at laboratory scale either during the final step of tertiary creep acceleration toward failure [*Voight*, 1988; *Amitrano and Helmstetter*, 2006], or as pure brittle failure in heterogeneous materials [*Guarino et al.*, 2002]. At the volcano scale, both processes are suggested to correspond to damage in the storage zone injection [*Collombet et al.*, 2003; *Grasso and Zaliapin*, 2004; *Traversa and Grasso*, 2009], which further allow injection of magma in the shallow volcanic edifice as a dyke pathway. It is also in agreement with the damage signature of multiple aborted dyke injections, which lead to the final route of a dyke intrusion toward free surface as a non-yet mature dyke injection, in an early percolation phase.

[39] This later dyke intrusion phase is well resolved by the increase of displacement rate on the eruption day, contemporary to huge constant seismicity rate recorded a few hours before eruption [*Peltier et al.*, 2005; *Traversa and Grasso*, 2009]. The displacement rate increases above background level only one or two days before eruption (Figure 8b), imaging strong localized deformations. Due to the one-day accuracy of the data sampling, it confirms that the accelerating pattern happens in the few hours preceding the eruption. It supports the last day crack opening rate to map the local deformation induced by the propagating dyke [e.g. *Toutain et al.*, 1992; *Peltier et al.*, 2005; *Peltier et al.*, 2006; *Battaglia and Bachèlery*, 2003].

[40] These results validate a three-step mechanism leading to magma transfers toward the surface as magma storage maturation, damage of the storage area, and dyke propagation.

5.2. Predictability of Eruptions Thanks to the Three Forerunners

[41] When applying the pattern recognition and error diagram analysis on the VT event rate of Piton de la Fournaise volcano (1988–2001), *Grasso and Zaliapin* [2004] showed that the best prediction results were obtained when averaging the daily seismicity rate over 5 days and issuing a prediction alarm for the next 5 days. Then 65% of the eruptions are predicted for an alarm time fraction smaller than 20%.

[42] When considering VT event rate on 1999–2006 period and the optimum point as defined in equation (2), we find slightly different results. The best prediction result is obtained for a time-window s = 1 day, when issuing an alarm for 41 days, with a threshold of 46 events per day. Such alarm parameters allow to predict more than 80% of the eruptions, with 40% of false alarm and an alarm duration of 42% of the time considered. This specific choice of alarm parameters allows more successful predictions than *Grasso and Zaliapin* [2004] results, however with a larger alarm time fraction.

[43] This work is a first attempt to quantify the predictive power for three forerunner on a same volcano. The seismicity rate resolves the minimum failure to predict rate, and the cumulative deformation allows the smallest D-value (equation (2)) when minimizing together the false alarm rate, the alarm duration and the failure to predict. We show that, even simple AND or OR rule to combine forerunners allow to improve the prediction results relatively to the one issued using each single forerunner independently. When considering the cumulative seismicity or the cumulative deformation, the optimum value decreases to 0.44 (against 0.50 for the cumulative deformation alone), corresponding to a missed event rate of 22%, a false alarm rate of 22% and an alarm time fraction of 30%. From Figure 6, the velocity changes are the noisiest observable and it may explain why the average decrease in velocity changes rate 50 days from eruptions (Figure 8) does not come out as a powerful forerunner (Figure 14). Accordingly, within the prediction strategy and the prediction scheme we use in this study, seismicity rate and crack opening data are the most efficient forerunners.

[44] These prediction outputs depend on the choice we made regarding the time function we analyzed, the pattern tested in the pattern recognition algorithm and the choice of prediction strategy. Many other data combinations are to be explored. The prediction strategy we chose is not unique and the exploration of the best prediction scheme remains the decision-makers choice. Given the context and the vulnerability, some might favor a maximal successful prediction rate, whatever the cost in terms of false alarms or alarm duration. In some cases, it might be more reasonable for societal impacts to minimize the number of false alarm rate. Because the error diagrams give all the possible prediction outcomes, it is a powerful tool for the decision-makers to adapt consequently weighting coefficients (equation (2)).

[45] Therefore, one major impact of this study is to demonstrate cross-analysing different kind of geophysical data leads to improve the predictive power, and to reduce the uncertainties in the volcanic hazard assessment. This cross-correlation of two or more geophysical or geochemical techniques in order to improve the assessment of volcanic activity is the very basis of daily working routine of volcano observatories. When in most observatories the cross-correlations of observable are on the basis of expert skills, our analysis quantifies the strict prediction power for the 3 sets of available data.

[46] As a next step to this work, the comparison between the performances of observatory routines and our "theoretical" approach could be performed. To our knowledge there is no information on the performances of the OVPF routines for prediction, which are expert based skills, especially on the 1999–2006 period. When the expert based skills would outperform our "theoretical" results, it would indicate that there are implicit information we failed to explicitly use in our prediction scheme. Either there would be additional information not included in the time series we used, or we would have failed to identify it through pattern recognition tools. As a final remark, one may note in this study that we only focused on time prediction, without any size nor space location for the ongoing eruptions, thus attesting a comprehensive eruption forecast is still a goal to be achieved.

[47] **Acknowledgments.** This work is supported by ANR Undervolc project. We are grateful to the Observatoire du Piton de la Fournaise (OVPF) for geophysical data of Piton de la Fournaise volcano.

References

Aki, K., and V. Ferrazzini (2000), Seismic monitoring and modeling of an active volcano for prediction, *J. Geophys. Res.*, *105*(B7), 16,617–16,640, doi:10.1029/2000JB900033.

Amitrano, D., and A. Helmstetter (2006), Brittle creep, damage and time to failure in rocks, *J. Geophys. Res.*, *111*, B11201, doi:10.1029/2005JB004252.

Bachèlery, P., and P. Mairine (1990), Evolution volcano-structurale du Piton de la Fournaise depuis 0.53 Ma, in *Le Volcanisme de la Réunion*, pp. 213–242, Cent. de Rech. Volcanogiques, Clermont-Ferrand, France.

Bachèlery, P., L. P. Ricard, T. Staudacher, P. Catherine, and P. Kowalski (2001), Extensometer variations, a refined precursor of volcanic eruptions, paper presented at XXVI General Assembly, Mars 2001, Eur. Geophys. Soc., Nice, France.

Battaglia, J. (2001), Seismic quantification of magmatic processes on the Piton de la Fournaise between 1991 and 2000, PhD thesis, Univ. de Paris 7, Paris.

Battaglia, J., and P. Bachèlery (2003), Dynamic dyke propagation deduced from tilt variations preceding the March 9, 1998, eruption of the Piton de la Fournaise volcano, *J. Volcanol. Geotherm. Res.*, *120*(3), 289–310.

Bell, A., and C. Kilburn (2012), Precursors to dyke-fed eruptions at basaltic volcanoes: Insights from patterns of volcano-tectonic seismicity at Kilauea volcano, Hawaii, *Bull.Volcanol.*, *74*, 325–339.

Brenguier, F., N.-M. Shapiro, M. Campillo, V. Ferrazzini, Z. Duputel, O. Coutant, and A. Nercessian (2008), Towards forecasting volcanic eruptions using seismic noise, *Nat. Geosci.*, *1*(2), 126.

Chouet, B.-A. (1996), Long-period volcano seismicity: Its source and use in eruption forecasting, *Nature*, *380*(6572), 309–316.

Collombet, M., J.-R. Grasso, and V. Ferrazzini (2003), Seismicity rate before eruptions on Piton de la Fournaise volcano: Implications for eruption dynamics, *Geophys. Res. Lett.*, *30*(21), 2099, doi:10.1029/2003GL017494.

Courtillot, V., J. Besse, D. Vandamme, R. Montigny, J.-J. Jaeger, and H. Cappetta (1986), Deccan flood basalts at the Cretaceous/Tertiary boundary?, *Earth Planet. Sci. Lett.*, *80*(3–4), 361–374.

Duputel, Z., V. Ferrazzini, F. Brenguier, N. Shapiro, M. Campillo, and A. Nercessian (2009), Real time monitoring of relative velocity changes using ambient seismic noise ar the Piton de a Fournaise volcano (La Réunion) form January 2006 to June 2007, *J. Volcanol. Geotherm. Res.*, *184*(1–2), 164–173.

Dzurisin, D., R.-Y. Koyanagi, and T.-T. English (1984), Magma supply and storage at Kilauea volcano, Hawaii, 1956–1983, *J. Volcanol. Geotherm. Res.*, *21*(3–4), 177–206.

Gillot, P.-Y., and P. Nativel (1989), Eruptive history of the Piton de la Fournaise volcano, Réunion Island, Indian Ocean, *J. Volcanol. Geotherm. Res.*, *36*(1–3), 53–65.

Grasso, J.-R., and P. Bachèlery (1995), Hierarchical organization as a diagnostic approach to volcano mechanics: Validation on Piton de la Fournaise, *Geophys. Res. Lett.*, *22*(21), 2897–2900.

Grasso, J.-R., and I. Zaliapin (2004), Predictability of volcano eruption: Lessons from a basaltic effusive volcano, *Geophys. Res. Lett.*, *31*, L05602, doi:10.1029/2003GL019022.

Guarino, A., S. Ciliberto, A. Garcimartın, M. Zei, and R. Scorretti (2002), Failure time and critical behaviour of fracture precursors in heterogeneous materials, *Eur. Phys.J. B*, *26*(2), 141–151.

Kagan, Y.-Y., and L. Knopoff (1981), Stochastic synthesis of earthquake catalogs, *J. Geophys. Res*, *86*(4), 2853–2862.

Kagan, Y.-Y., and L. Knopoff (1987), Statistical short-term earthquake prediction, *Science*, *236*(4808), 1563–1563.

Keilis-Borok, V. (2002), Earthquake prediction: State-of-the-art and emerging possibilities, *Annu. Rev. Earth Planet. Sci.*, *30*(1), 1–33.

Kilburn, C.-R.-J. (2003), Multiscale fracturing as a key to forecasting volcanic eruptions, *J. Volcanol. Geotherm. Res.*, *125*(3–4), 271–289.

Klein, F.-W. (1984), Eruption forecasting at Kilauea volcano, Hawaii, *J. Geophys. Res.*, *89*(B5), 3059–3073.

Lahaie, F., and J.-R. Grasso (1998), A fluid-rock interaction cellular automaton of volcano mechanics: Application to the Piton de la Fournaise, *J. Geophys. Res.*, *103*(B5), 9637–9649.

Lemarchand, N., and J.-R. Grasso (2007), Interactions between earthquakes and volcano activity, *Geophys. Res. Lett.*, *34*, L24303, doi:10.1029/2007GL031438.

Lenat, J.-F., and P. Bachèlery (1987), Dynamic of magma transfer at Piton de la Fournaise volcano (Réunion Island, Indian Ocean), in *Earth Evolution Sciences–Special Issue "Modeling of Volcanic Processes"*, pp. 57–72, Friedr. Vieweg, Brauschweig, Germany.

Marzocchi, W., and L. Zaccarelli (2006), A quantitative model for the time-size distribution of eruptions, *J. Geophys. Res.*, *111*, B04204, doi:10.1029/2005JB003709.

Marzocchi, W., L. Sandri, P. Gasparini, C. Newhall, and E. Boschi (2004), Quantifying probabilities of volcanic events: The example of volcanic hazard at Mount Vesuvius, *J. Geophys. Res.*, *109*, B11201, doi:10.1029/2004JB003155.

Marzocchi, W., L. Sandri, and J. Selva (2008), Bet_ef: A probabilistic tool for long-and short-term eruption forecasting, *Bull. Volcanol.*, *70*(5), 623–632.

McGuire, W.-J., and C.-R.-J. Kilburn (1997), Forecasting volcanic events: Some contemporary issues, *Geol. Rundsch.*, *86*(2), 439–445.

McNutt, S. (1996), Seismic monitoring and eruption forecasting of volcanoes: A review of the state-of-the-art and case histories, in *Monitoring and Mitigation of Volcano Hazards*, pp. 99–146, Springer, New York.

McNutt, S.-R. (2002), Volcano seismology and monitoring for eruptions, in *International Handbook of Earthquake and Engineering Seismology*, *Int. Geophys. Ser.*, vol. 81, pp. 383–406, Academic, Amsterdam.

Melnik, O., and R.-S.-J. Sparks (1999), Nonlinear dynamics of lava dome extrusion, *Nature*, *402*(6757), 37–41.

Merle, O., P. Mairine, L. Michon, P. Bachèlery and M. Smietana (2010), Calderas, landslides and paleo-canyons on Piton de la Fournaise volcano (La Réunion Island, Indian Ocean), *J. Volcanol. Geotherm. Res*, *189*, 131–142.

Minakami, T. (1960), Fundamental research for predicting volcanic eruptions (Part 1). Earthquakes and crustal deformations originating from volcanic activities, *Bull. Earthquake Res. Inst*, *38*, 497–544.

Molchan, G.-M. (1997), Earthquake prediction as a decision-making problem, *Pure Appl. Geophys.*, *149*(1), 233–247.

Mulargia, F., S. Tinti, and E. Boschi (1985), A statistical analysis of flank eruptions on Etna volcano, *J. Volcanol. Geotherm. Res.*, *23*(3–4), 263–272.

Mulargia, F., P. Gasperini, and W. Marzocchi (1991), Pattern recognition applied to volcanic activity: Identification of the precursory patterns to Etna recent flank eruptions and periods of rest, *J. Volcanol. Geotherm. Res.*, *45*(3–4), 187–196.

Mulargia, F., W. Marzocchi, and P. Gasperini (1992), Statistical identification of physical patterns which accompany eruptive activity on Mount Etna, Sicily, *J. Volcanol. Geotherm. Res.*, *53*(1–4), 289–296.

Peltier, A., V. Ferrazzini, T. Staudacher, and P. Bachèlery (2005), Imaging the dynamics of dyke propagation prior to the 2000–2003 flank eruptions at Piton de la Fournaise, Reunion Island, *Geophys. Res. Lett.*, *32*, L22302, doi:10.1029/2005GL023720.

Peltier, A., T. Staudacher, P. Catherine, L.-P. Ricard, P. Kowalski, and P. Bachèlery (2006), Subtle precursors of volcanic eruptions at Piton de la Fournaise detected by extensometers, *Geophys. Res. Lett.*, *33*, L06315, doi:10.1029/2005GL025495.

Peltier, A., F. Massin, P. Bachèlery, and A. Finizola (2012), Internal structure and building of basaltic shield volcanoes: The example of the Piton de La Fournaise terminal cone (La Réunion), *Bull. Volcanol.*, *74*(8), 1881–1897.

Sandri, L., W. Marzocchi, and P. Gasperini (2005), Some insights on the occurrence of recent volcanic eruptions of Mount Etna volcano (Sicily, Italy), *Geophys. J. Int.*, *163*(3), 1203–1218.

Sapin, M., A. Hirn, J. Lépine, and A. Nercessian (1996), Stress, failure and fluid flow deduced from earthquakes accompanying eruptions at Piton de la Fournaise volcano, *J. Volcanol. Geotherm. Res.*, *70*(3–4), 145–167.

Sparks, R.-S.-J. (2003), Forecasting volcanic eruptions, *Earth Planet. Sci. Lett.*, *210*(1–2), 1–15.

Stieltjes, L., and P. Moutou (1989), A statistical and probabilistic study of the historic activity of Piton de la Fournaise, Réunion Island, Indian Ocean, *J. Volcanol. Geotherm. Res.*, *36*(1–3), 67–86.

Toutain, J., P. Bachèlery, P. Blum, J. Cheminee, H. Delorme, L. Fontaine, P. Kowalski, and P. Taochy (1992), Real time monitoring of vertical ground deformations during eruptions at Piton de la Fournaise, *Geophys. Res. Lett.*, *19*(6), 553–556.

Traversa, P., and J.-R. Grasso (2009), Brittle creep damage as the seismic signature of dyke propagations within basaltic volcanoes, *Bull. Seismol. Soc. Am.*, *99*(3), 2035.

Turner, M.-B., S.-J. Cronin, M.-S. Bebbington, and T. Platz (2008), Developing probabilistic eruption forecasts for dormant volcanoes: a case study from Mt Taranaki, New Zealand, *Bull. Volcanol.*, *70*(4), 507–515.

Vinciguerra, S., V. Latora, S. Bicciato, and R.-T. Kamimura (2001), Identifying and discriminating seismic patterns leading flank eruptions at Mt. Etna Volcano during 1981–1996, *J. Volcanol. Geotherm. Res.*, *106*(3–4), 211–228.

Voight, B. (1988), A method for prediction of volcanic eruptions, *Nature*, *332*, 125–130.

Wadge, G., and M.-C. Isaacs (1988), Mapping the volcanic hazards from Soufriere Hills volcano, Montserrat, West Indies using an image processor, *J. Geol. Soc.*, *145*(4), 541.